Background simulation for a balloon-borne gas scintillation proportional counter

D. A. Swartz,[a] Y. Z. Chen,[b] and B. D. Ramsey[c]

[a]Universities Space Research Association
Huntsville, AL 35812 USA

[b]University of Alabama at Huntsville
Huntsville, AL 35805 USA

[c]NASA/Marshall Space Flight Center
Huntsville, AL 35812 USA

ABSTRACT

Numerical simulations are used to predict the cosmic-ray-induced background in a passively-shielded gas scintillation proportional counter. A pair of these detectors will be flown as focal plane instruments for a hard x-ray telescope balloon-borne experiment. The investigation begins with one-dimensional transmittance studies to determine optimum thickness and composition for additional passive shielding. These simulations suggest, within weight and other design constraints, 0.3 cm of lead would reduce shield leakage within the detector by an order of magnitude over the ~40-200 keV range while adding only negligibly to photon production within the shielding mass by hadronic interactions. Simulations of the entire as-built detector, on the other hand, predict this added shielding reduces shield leakage by only ~40% and the total background rate (including shield leakage and production but ignoring aperture flux) by only ~27%. The discrepancy between one-dimensional and full detector results is attributed to multiple Compton scattering of unattenuated hard x-rays within the pressure vessel which reduces initial photon energies to within detectable bounds and to leakage and production in the attached, unshielded, electronics housing. The aperture flux can be reduced by 90% by adding an aperture collimator for a final (shielded and collimated) detector total background in the 15-50 keV operating range of ~0.0043 cts-s^{-1}-cm^{-2}-keV^{-1}; a 65% reduction compared to the as-built detector. The dominant source of background remains cosmic diffuse and atmospheric gamma-ray leakage through the radiation shields and thin pressure vessel walls with a minor photon production contribution. Although this rate is higher than typically attained using active shielding techniques, a high S/N ratio is achieved by the combined telescope-detector system.

1. INTRODUCTION

A pair of gas scintillation proportional counters (GSPC) has been built as part of the ongoing x-ray instrumentation development program at MSFC. These detectors will serve as focal plane instruments for the first balloon flight test of a hard x-ray telescope system operating in the 15-50 keV energy band. The as-built detector is protected from penetrating radiation only by its Stainless Steel pressure vessel walls. It contains no active shielding. As a consequence, background noise is expected to be high although mitigated by the focusing optics and imaging capabilities of the detector.

Therefore, in addition to development and testing of the detector hardware[1] and x-ray optics systems[2,3] reported elsewhere, numerical simulations have been conducted to provide quantitative estimates of the cosmic ray-induced background expected in flight and to investigate possible background-reducing strategies. The fact that the detector has already been built, in addition to leadtime, cost, and weight constraints, limits the potential background-reducing measures that can be taken. Specifically, the only changes in the design considered here are addition of passive shielding to reduce shield leakage and installation of a collimator to reduce aperture flux.

in *X-Ray and Gamma-Ray Instrumentation for Astronomy XI*, K. A. Flanagan and O. H. W. Siegmund, eds., *Proc. SPIE* **4140**, 2000.

D.A.S.: Doug.Swartz@msfc.nasa.gov; 256-544-5500.
Y.Z.C: chenyz@jet.uah.edu; 256-890-6276.
B.D.R: Brian.Ramsey@msfc.nasa.gov 256-544-7743.

Analysis begins (§ 3) with one-dimensional transmittance studies of slabs of different thicknesses and compositions in conjunction with realistic external radiation environment models. According to these one-dimensional "slab" studies, the detector walls are nearly transparent to background photons above about 40 keV with a peak intensity at 90 keV but are only a weak site of photon production. This suggests additional shielding may be beneficial. The optimum shielding, within weight limitations, is shown to be 0.3 cm of Pb. Greater thicknesses do not further reduce shield leakage above ∼100 keV but do increase low-energy photon production by neutrons and protons. Lesser thicknesses transmit strong Pb K-α and K-β fluorescence lines which are self-absorbed in the 0.3 cm case.

One-dimensional transmittance models do not address multiple interactions within the detector housing walls and internal structures, production in and penetration through nearby payload masses, nor the proportion of flux through the finite aperture. These and related issues are addressed using numerical simulations of the entire detector in § 4. Results from three full models are presented: the as-built detector, the detector with a collimator to limit the open solid angle, and a model of the detector with collimator and a 0.3-cm-layer of additional Pb shielding.

All three designs yield a background level (ignoring the aperture flux component in the as-built case) of ∼6.6-9.1 cts-s^{-1} in the 123 cm^3 active volume. Such a small active volume is possible, of course, because the detector will be used in conjunction with focussing x-ray optics. Still, the shield leakage dominates the background at energies of interest and the additional shielding reduces this component only moderately. The reduction is not as large as predicted by the one-dimensional transmittance studies because, although the direct flux of photons in the detector's sensitive energy range is reduced, penetrating harder photons, and those generated by hadron interactions, undergo multiple inelastic scattering within the detector and nearby electronics enclosure and are subsequently absorbed in the sensitive volume. Thus the additional shielding does not reduce the detected background significantly though it does attenuate soft incident x-rays.

Section 2 describes the detector model, the external radiation environment, and the numerical methods used in the simulations. Results of one-dimensional slab simulations are presented in § 3 and of full detector simulations in § 4. Section 5 summarizes these results and discusses the implications for improving sensitivity.

2. SIMULATION METHODS

2.1. Detector Configuration

The detector,[1] shown schematically in figure 1, consists of a 0.3-cm-thick cylindrical stainless steel pressure vessel, roughly 14 cm diameter and 15.5 cm high, filled with xenon gas at 10 atmospheres. The top face of this vessel is a 0.7-cm-thick Stainless Steel disk with a 5-cm-diameter circular entrance aperture. The bottom face is 2.1 cm thick Stainless Steel with a 0.7-cm-thick UV-transmitting circular window (7.6 cm diameter) coupling the pressurized gas chamber above with a position-sensitive photo-multiplier tube below. The absorption and drift region and the scintillation region together comprise a cylinder of radius 5 cm extending 6.25 cm above the UV window. Above this active Xe region are two beryllium entrance windows (the outer window hermetically seals the inner window to prevent electrical discharge while the inner window is held at a negative high voltage) with the intervening space filled with nitrogen at atmospheric pressure. An array of field shaping rings surrounds the cylindrical side of the active volume. This array is modeled as a cylindrical shell of ceramic representing the insulating material filling the space between the shaping rings. The pressure vessel contains other ceramic and Stainless Steel structures, as illustrated. The photo-multiplier tube and all electronics are housed within a 25x25x36 cm aluminium box (shown only in part) mounted below the pressure vessel. The electronics within this box are modeled as reduced-density aluminium.

The detector is designed to be most sensitive in the 15-75 keV hard x-ray band between the low-energy atmospheric photon cutoff at balloon altitudes and the high energy cutoff of Ir-coated grazing incidence mirrors. Test mirrors, with a cutoff nearer to 50 keV, will be used in the upcoming engineering flight.

2.2. External Radiation Environment

The flux spectra of the external sources are shown in figure 2. The diffuse cosmic and atmospheric gamma-rays are represented by a power law, $dN/dE = 9.2E^{-1.78}$ photons-cm^{-2}-s^{-1}-keV^{-1}-str^{-1}, above a cutoff at $E = 10$ keV. This spectrum is based upon the parameterization given[4] for a residual atmosphere of 3.5 g-cm^{-2} for a flight from Ft. Sumner, NM (latitude 34.5° N) and allows approximately for variation with zenith angle. The atmospheric cutoff is closer to 20 keV at float altitude but gamma-rays at this and lower energies are photoelectrically absorbed

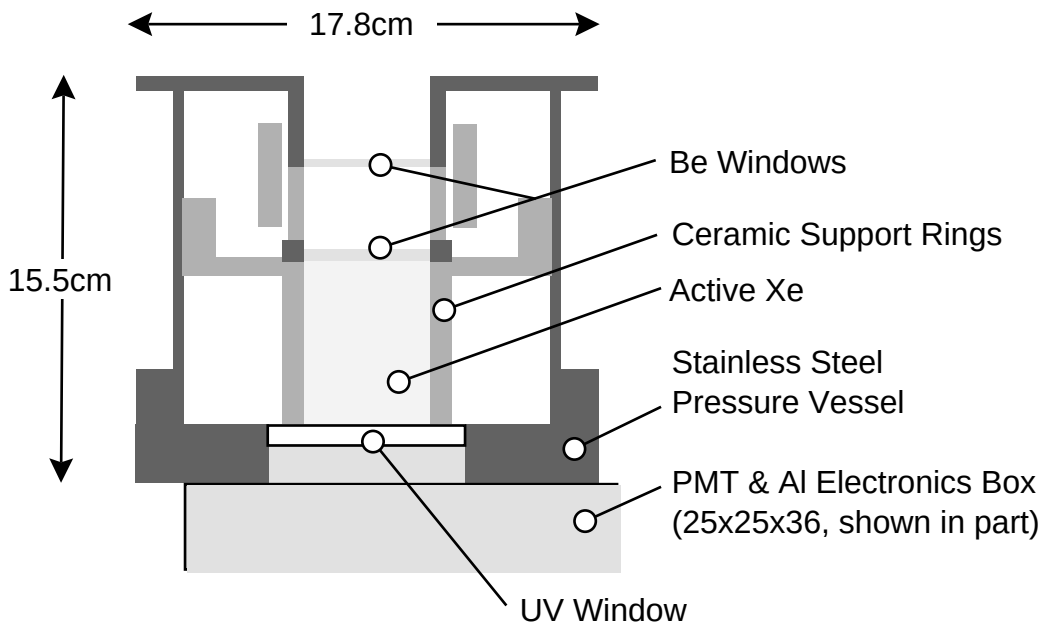

Figure 1. Schematic view of the main body of the GSPC showing a plane cross-section through the axis of cylindrical symmetry. The outer Stainless Steel walls comprise the pressure vessel. Field shaping ring supports are modeled as ceramic slabs. Source photons enter from above through the Be windows and are absorbed in the active Xe volume. Scintillation photons emerging from the bottom of the active Xe chamber pass through the UV-transmitting window and are imaged by a photo-multiplier tube (PMT) located within the Al electronics housing.

before reaching the active volume (except for those passing through the aperture) so that extending the incident spectrum down to 10 keV has minimal effect on our results. The cosmic ray proton component is also a power law, $dN/dE = 0.073E^{-1.8}$ protons-s^{-1}-cm^{-2}-keV^{-1}-str^{-1}, with a geomagnetic cutoff at 3.6 GeV. The ambient neutron flux spectrum resulting from cosmic ray interactions in Earth's atmosphere is approximated by a broken power law[5]: $dN/dE = 10^{12}E^{1}$ for $E \leq 10^{-7}$ MeV; $dN/dE = 0.069E^{-0.88}$ for $10^{-7} < E \leq 60$ MeV; and $dN/dE = 5.75E^{-1.94}$ for $E > 60$ MeV, all in units of neutrons-s^{-1}-cm^{-2}-keV^{-1}-str^{-1}. The spectrum includes low-energy thermal neutrons which can readily penetrate the detector and produce de-excitation gamma-ray emission following neutron capture. All three source components are zenith-angle dependent but are assumed isotropic in the present study for computational expediency. For instance, the neutron flux varies by perhaps a factor of 2 or more with zenith angle[6] depending on energy but with considerable uncertainty.

Atmospheric protons, with a spectral dependence[7] similar to that of atmospheric neutrons, are not treated explicitly. Numerical experiments analogous to those reported in § 3 indicate the production of photons, neutrons, and charged particles by atmospheric protons is typically $\lesssim 10\%$ that of galactic cosmic-ray protons at all energies with the exception of protons in the ∼10 to 100 MeV range where atmospheric protons exceed galactic by a factor of ∼2. No other background sources are included in the present study.

2.3. Numerical Method

Photon and particle transport is simulated using the GEANT[9] Monte Carlo program. The GEANT/MICAP[10] interface is used to model interactions of neutrons below 20 MeV and GEANT/FLUKA[11] is used at higher kinetic energies and for protons.

A complete simulation consists of three parts corresponding to the three external sources described above. Particle transport histories are initiated by randomly sampling initial position, direction, and energy. The initial position coincides with a point on the minimal rectangular box enclosing the pressure vessel, electronics box, and collimator. For the one-dimensional slab models, the initial position is simply the outer surface of the slab. The initial energy is sampled from the adopted energy spectra defined in section 2.2.

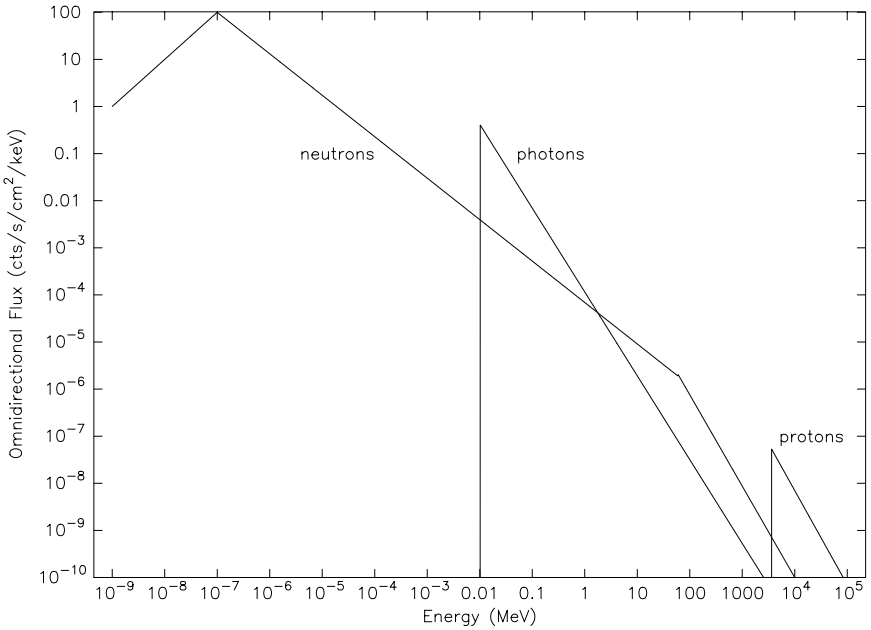

Figure 2. External source spectra adopted for the simulations reported in § 3 and § 4. Float altitude is 39 km at latitude 34.5° N.

The initial particles and all secondary particles and photons created during each history are fully transported through the detector model until they either escape the volume (or the inner surface for slab models) or are terminated. Termination occurs, numerically, whenever a particle is destroyed, falls below preset energy thresholds, or, in the case of charged particles, enters the active Xe volume. The latter case is included because it is assumed that charged particles entering the Xe volume will deposit an amount of energy greater than the upper threshold trigger which is set by on-board electronics to an energy just above that of the mirror cut-off, ∼75 keV. This assumption, discussed in § 4.2, is checked in post-processing by computing the energy deposited in the active volume from the terminated particle's energy, position, and direction in the continuous-slowing-down-approximation. Transport of photons, neutrons and other neutral particles is not terminated in this manner. The preset energy thresholds used in this work are the default GEANT values of ∼10 keV for all particles and photons with the exception of neutrons. The neutron low-energy cutoff is set to 10^{-3} eV in order to accurately simulate the response to slow, thermal neutrons.

Each history can produce zero or more events. Events are defined as the deposition of energy within the active Xe volume. A data record is written for each event. Events are analyzed in post-processing to determine what the true electronic signature of the events would be. All events associated with a given history (initial particle) are assumed to occur simultaneously; so, for instance, the energies deposited by such events are summed in post-processing to obtain the total energy detected for that history, and this is the quantity reported in this work. This might lead to on-board rejection of the history if this energy exceeds the upper threshold trigger. The detector has the ability, however, to distinguish spatially-separated events which may indicate a true photon detection (such as photoionization with subsequent absorption of the fluorescent photon elsewhere in the active volume) or multiple events (detection, for instance, of two discreet bremsstrahlung photons generated by a proton passing through the electronics enclosure). Thus, the event position, incident particle type and direction, and the types and directions of any particles generated in the event are also recorded for further analysis.

Only prompt background events are considered; the delayed background due to decay emissions from material activation is expected to be negligible during the relatively short balloon flight.

3. SLAB SIMULATIONS

One-dimensional slab models illustrate most simply the relationship between the transmittance properties of the detector materials and the detected background signature. Once the spectral signatures from the individual cosmic

ray components are understood as functions of slab composition and depth, the models can be extended to investigate possible choices for additional passive shielding.

Consistent with these goals, and considering payload weight limitations, an investigation of the transmittance properties of the as-built Stainless Steel pressure vessel was undertaken. The composition of Stainless Steel is approximated as pure iron. The wall thicknesses range from the 0.3 cm cylindrical side to the 2.1 cm bottom flange (figure 1). Additional shielding materials considered are tin and lead and combinations of these materials, overlying the Fe. Tin and lead are common materials used for passive shielding because they are inexpensive and easily shaped to conform to the contours of the detector. The full set of one-dimensional simulations performed are listed in table 1. The additional mass required to shield the cylindrical side and top of the existing pressure vessel for the additional shielding models is also given in the table. The mass added varies approximately as $M \propto \rho t$ for thin shield layers where ρ is the shield mass density and t the shield thickness.

Table 1 One-dimensional Slab Models

material	model material	density (g/cm^3)	thicknesses, t (mm)	mass added (kg)
316 Stainless	^{26}Fe	7.87	3, 5, 9, 13, 15, 21, 25, 30, 35, 40	–
Fe/Tin	^{50}Sn	7.87/7.31	3/5, 3/10, 3/15	0.82/mm
Fe/Lead	^{82}Pb	7.87/11.35	3/1, 3/3, 3/5, 7/1, 7/3, 7/5	1.3/mm
Fe/Sn/Pb	^{82}Pb	7.87/7.31/11.35	3/1/1, 3/3/1, 3/5/1	1.3+0.82/mm

Figure 3 displays the shield leakage and photon production fluxes emergent into 2π steradians from the side opposite the irradiated surface of two Stainless Steel slab models representing the range of pressure vessel wall thicknesses in the as-built detector.

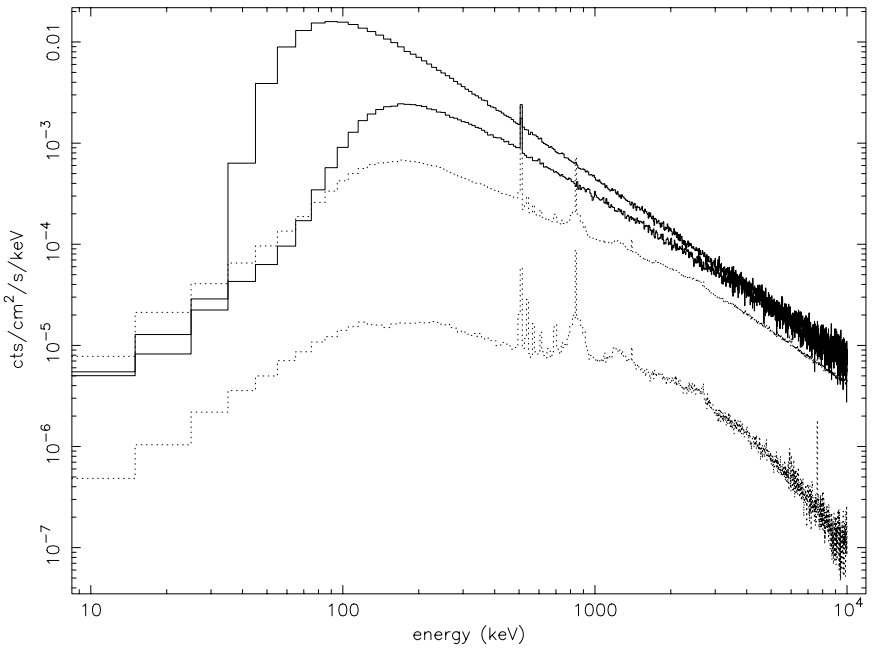

Figure 3. Shield leakage (solid lines) and photon production spectra (dotted lines) for two slab thicknesses representing the range of Stainless Steel pressure vessel wall thicknesses: $t = 0.3$ cm: upper solid line and *lower* dotted line; $t = 2.1$ cm: lower solid line and *upper* dotted line. (Photon production increases and shield leakage decreases as wall thickness increases.)

The shield leakage contribution (i.e., the transmitted atmospheric and diffuse cosmic gamma-ray background component) dominates the flux: The spectra display the characteristic shape of a photoelectrically absorbed power law. The low level flux below the photoelectric cutoff is caused by the redistribution of hard x-rays (typically,

$E \gtrsim 100$ keV) to lower energies by inelastic (Compton) scattering within the slab. The photoelectric cutoff shifts toward higher energies as the slab thickness increases but there remains a high shield leakage contribution above $E \sim 100$ keV and the slab is effectively transparent above $E \sim 1$ MeV.

Photons produced by cosmic ray protons and atmospheric neutrons contribute a broad photon continuum with numerous prompt nuclear de-excitation lines and the pair annihilation line superimposed. These photons contribute substantially to the total photon flux at low energies because, whereas soft photons incident upon the outer surface are efficiently attenuated, photons produced within the slab itself encounter a smaller outward optical depth and can escape the slab. The spectral shape of the photon production component varies only weakly with slab thickness in contrast with the shield leakage component. Neutrons and protons produce similar photon spectra with neutrons contributing $\sim 50\%$ of the total photon production counts at $t = 0.3$ cm but only $\sim 25\%$ at $t = 2.1$ cm.

These general trends are repeated for all slab models computed with thicknesses less than a few centimeters. Photon production becomes more important at ever higher energies as the slab thickness is increased. The shield leakage component is modified only slightly by increasing slab thickness: the spectral peak shifts towards higher energies and the flux at this peak is slightly reduced. Meanwhile, photon production increases exponentially with slab thickness. Hence, there will be an optimum shield thickness above which increased production will outweigh increased attenuation.

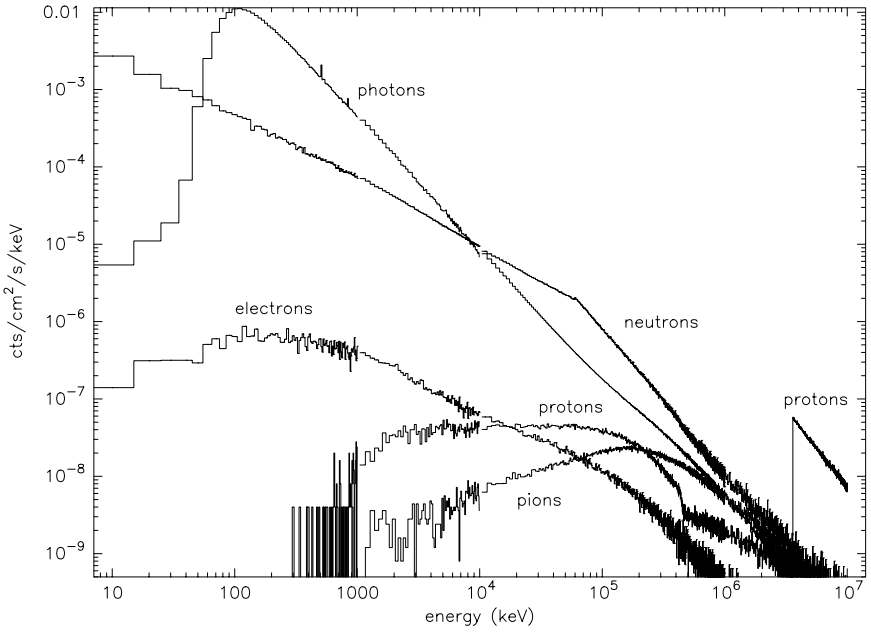

Figure 4. Particle flux emerging from 0.7 cm thickness of Fe representing the area-weighted average pressure vessel wall thickness.

Particles other than photons are also produced within the slab and, of course, many of the energetic incident particles pass through the slab. Figure 4 displays the total flux spectrum of those particles most commonly emerging from a 0.7 cm Stainless Steel slab model, summed over all three external (flight) source components. In addition to a photon spectrum analogous to that discussed above, there is a significant flux of neutrons and electrons extending to low energies, and protons and pions at energies $E > 1$ MeV. The neutron spectrum is nearly identical to the incident neutron spectrum indicating most of the neutrons pass through the slab unattenuated. Similarly, a power law proton component is evident above the geomagnetic cutoff at $E = 3.6$ GeV. Electrons (and similarly, though not shown, positrons) form a flat spectrum below $E \sim 10$ MeV. Charged particles are considered in more detail in section 4.2 where the associated detected events are discussed for the full detector models.

Photons clearly dominate the potential background in the GSPC and shield leakage is the greatest source of these photons. Photons entering the pressure vessel must also pass through the "dead layer" of Xe between the pressure

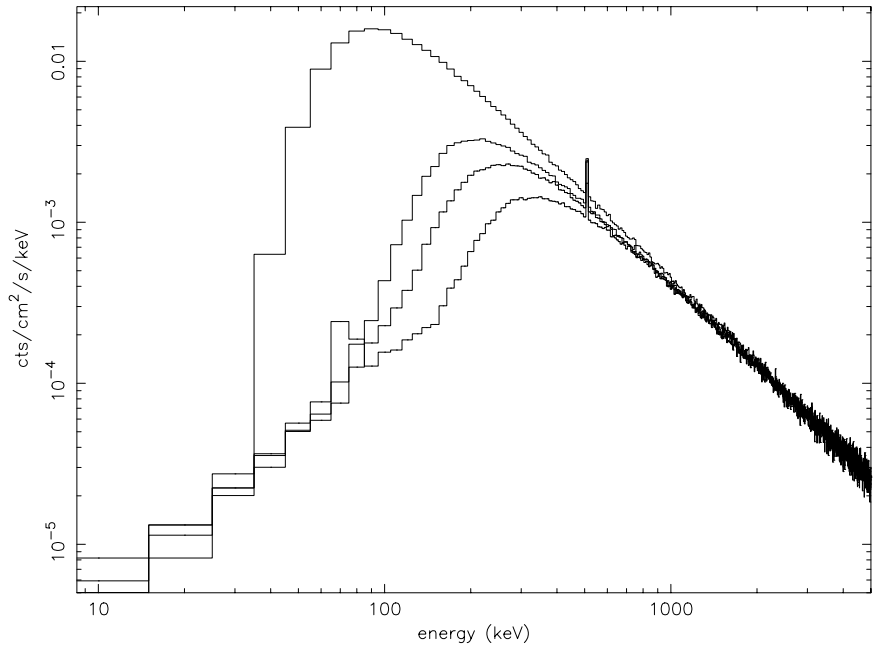

Figure 5. Total photon flux spectra emergent from several representative shielding configurations. External particles and photons emerge from the Sn and/or Pb shielding before encountering the underlying Fe pressure vessel slab. Shown, top to bottom are: (*i*) Unshielded 0.3 cm Fe, (*ii*) 0.3 cm Fe with 0.5 cm Sn, (*iii*) 0.3 cm Fe with 0.5 cm Sn and 0.1 cm Pb, and (*iv*) 0.3 cm Fe with 0.3 cm Pb shielding. Note the Pb-Kα line at 75 keV.

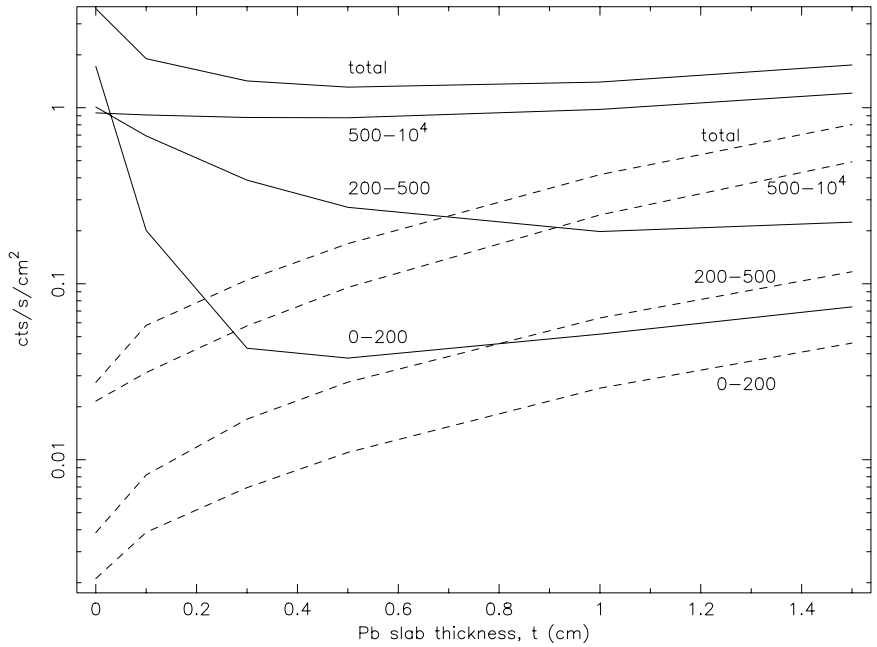

Figure 6. Dependence of photon flux in several x-ray bands on additional Pb shielding thickness. The $t = 0$ case corresponds to 0.3 cm Fe with no additional Pb shielding. Curves are labeled by energy band limits (in keV). Dashed lines display the photon production flux and solid lines represent total fluxes including shield leakage. Hard x-ray bands are unaffected by shielding while softer bands may reach a minimum before photon production causes an increase in the total flux.

vessel walls and the field-shaping array (figure 1). Soft x-rays will be photoelectrically absorbed in this layer (while low-energy charged particles thermalize through ionization losses). Thus, photons at energies $E \gtrsim$ 50-100 keV are the primary candidates for producing background events while the majority of much harder photons should pass through the active region undetected. The addition of passive shielding can potentially reduce this shield leakage component. High-Z materials are preferred because photons are efficiently removed only by photoionization and the photoionization opacity exceeds the Compton scattering opacity at the energies of interest only for high-Z materials. Conversely, high-Z materials are more likely sites of hadronic interactions leading to photon (and particle) production.

Figure 5 illustrates the effect of additional shielding. The total photon flux emergent from one-dimensional slabs of 0.3 cm Fe, representing the thinnest pressure vessel wall, with and without additional slabs of Sn and-or Pb are shown. The photon flux is significantly reduced in the energy band 50 $\lesssim E \lesssim$ 500 keV for all shielding combinations. The most effective, however, is simply a layer of Pb. None of the examples shown have a substantial photon production contribution. Enhanced photon production would appear as a flux increase in the low energy channels. This does not arise because the Fe layer "below" the high-Z slabs efficiently absorbs these soft photons while photon production at higher energies is compensated by the substantial reduction in shield leakage.

The optimal shielding thickness can be determined qualitatively from the full set of models listed in table 1 by first determining the minimum flux in the energy band of interest and then selecting the least mass increase configuration. This is illustrated in figure 6 for the case of Pb shielding where the photon flux in various spectral bands is shown against the slab thickness. The flux in the low energy channel, 0-200 keV, rapidly approaches a minimum at $t \sim$0.5 cm but increases for thicker slabs because of photon production. Harder bands show little or no dependence on shield thickness, slabs being more transparent to harder photons, although the photon production component increases exponentially as the shield thickness increases.

These conclusions were found to be true for all the models: The best flux reduction occurs for thin slabs, the reduction is primarily in the 100-500 keV range, and the photon production flux increases in all energy bands as the slab thickness increases. The optimal reduction was found for the case of Pb at $0.3 \leq t \leq 0.5$ cm.

4. DETECTOR SIMULATIONS

Having established the potential advantage of additional passive shielding based on one-dimensional slab simulations, it remains to select a shielding configuration and consider the full three-dimensional aspects of the detector. Three full detector model simulations were performed to estimate the background noise and to investigate possible background-reducing options. They are: (1) the as-built detector with only the existing pressure vessel providing shielding, (2) the detector with a 15 cm high, 0.3 cm thick, Stainless Steel collimator, and (3) the detector-collimator combination with the addition of 0.3 cm of Pb enclosing the cylindrical side and top of the pressure vessel.

The results of the previous section provided the basis for choosing the 0.3 cm Pb slab as an additional passive shield. The opening solid angle (figure 1) is 0.4 steradian producing a direct aperture flux of $\sim$0.43 photons-s^{-1}-cm^{-2} in the energy band $15 \leq E \leq 75$ keV assuming an $E^{-1.78}$ power law (see § 2.2). The 3-meter-focal-length telescope assembly allows a much smaller field of view. Extending a 5 cm OD cylindrical tube 15 cm above the top face of the pressure vessel will reduce the open solid angle to 0.03 steradians. The mass added is 0.56 kg if this collimator is composed of 0.3 cm thick Stainless Steel.

4.1. Radiation Background

The quantitative result of these simulations is the spectrum of energy deposited in the active Xe volume. The detected energy spectrum is obtained by summing the energy deposited by all events associated with a history then registering by incrementing the counts in the nearest energy bin. Deposited energy includes all atomic relaxation energies and the energy of any secondary charged particle produced (mainly recoil and Auger electrons) within the active Xe volume. If a charged particle *enters* the active volume, then the entire history is rejected and not included in the detected energy spectrum because large energy depositions in the active volume will automatically trigger an on-board rejection of further processing of the event. This issue is discussed further in § 4.2.

The left panel of figure 7 shows the individual contributions to the detected energy spectrum for the GSPC model with collimator and 0.3 cm Pb shielding added. The energy resolution adopted for this and subsequent spectra is arbitrary and does not account for instrumental broadening which has been measured to be $\sim$5% at 22 keV.[1] A resolution adequate to resolve line-like features and edges in the detected spectra is adopted here.

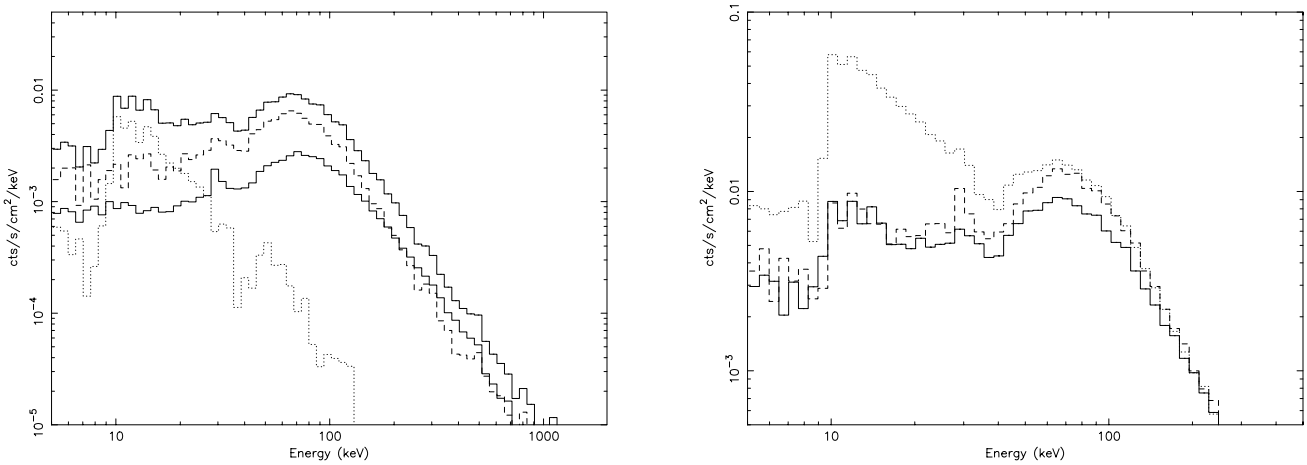

Figure 7. *Left:* Energy deposition spectrum for the GSPC detector with collimator and added shielding showing the contributions from shield leakage (dashed line), aperture flux (dotted line), photon production via hadronic interactions (lower solid line), and total flux (upper solid line). *Right:* Energy deposition spectra for the as-built GSPC (dotted line), with the addition of a collimator (dashed line), and with the addition of a collimator and 0.3 cm Pb shielding on the cylindrical side and top face of the detector main body (solid line).

Diffuse cosmic and atmospheric gamma-rays (shield leakage and aperture flux) dominate the detected spectrum at all energies. Xenon K line emission features appear in the spectra at ∼30 keV, caused by detection of fluorescence photons emitted from the Xe dead layer surrounding the active volume. The edge evident in the aperture flux spectrum just above the Xe K-edge at 35 keV is caused by fluorescence escapes following photoionization and resulting in incomplete charge collection. The aperture flux spectrum accurately mimics the external photon source from the low-energy cutoff at 10 keV (§ 2.2) to ∼60 keV but declines more rapidly than $E^{-1.78}$ at higher energies due to the increasing transparency of the 6.25 cm-deep active volume. This component provides ∼50% or more of the soft x-ray flux below $\lesssim$20 keV. As the true atmospheric cutoff is closer to 20-35 keV, as discussed in § 2.2, the predicted aperture flux shown here is an overestimate below this cutoff.

The right-side panel of figure 7 displays the total spectra for all three models. The high flux between 10 and 40 keV in the as-built model is aperture flux. Aside from this component, the three spectra are remarkably similar. A weak aperture flux component is still seen in the two models with a collimator at the expected level corresponding to the reduced solid angle subtended (∼92.5% reduction). Aperture flux accounts for all the differences between the two unshielded models with and without collimator below the 65 keV peak. The shielded model has the same aperture flux as does the collimated model without shielding. The shield leakage component is reduced 40% by the added shielding while photon production increases by 35% for a net reduction of ∼27% over the 15-50 keV band in the model with shielding compared to the collimated model without shielding.

The spectra displayed in figure 7 differ qualitatively from the one-dimensional slab models of section 3. One difference between these results is, of course, aperture flux which is not part of the one-dimensional models. Similarly, there is an energy deposition component from photons incident from the unshielded directions below the active volume, either through the bottom flange or through the UV-transmitting window and hence passing through or originating in the electronics enclosure.

Another factor that accounts for major differences between slab model and full model results can be explained by examination of figure 8 which displays the deposited shield leakage component from figure 7 along with the initial spectrum of detected photons and the spectrum of those same photons as they were incident upon the active volume. The initial spectrum of detected photons (dotted curve in figure 8) is that of an absorbed $E^{-1.78}$ power law qualitatively similar to the slab model shield leakage spectra, e.g., figure 3. However, these initial photons loose a considerable fraction of their energy before entering the sensitive volume as indicated by the shift of this relatively

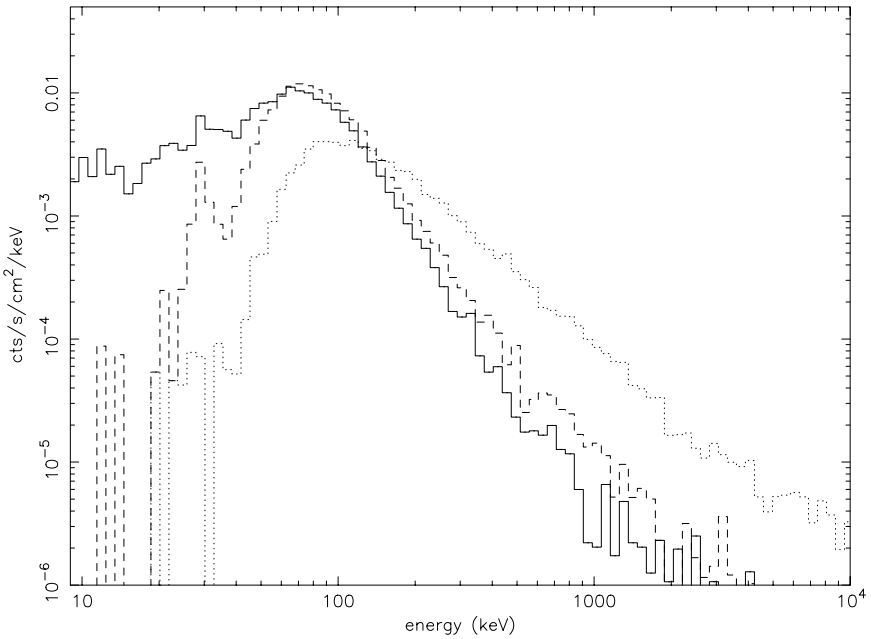

Figure 8. Spectra of the detected photons as they are incident upon the outside of the as-built detector (dotted line), as they are incident upon the detector sensitive volume (dashed line), and as they are finally detected through energy deposition within the sensitive volume (solid line).

hard initial spectrum to the softer spectrum of photons incident upon the active volume (dashed curve). This trend indicates hard x-rays undergo inelastic scattering before entering the active region. There is a second characteristic shift in the spectral shape seen when comparing the spectrum incident on the active volume to the detected energy spectrum. The hard x-ray band becomes, again, softer; and the low energy band below $E \sim$40 keV becomes much stronger. Again, this difference is due to Compton scattering of the hard photons and K-escapes of softer photons near the 65 keV peak which fills in the softest spectral channels.

Thus, a major difference between the results of this section and the slab models of § 3 is that the one-dimensional models estimate the transmittance through the slabs but do not account for the detection efficiency of the Xe gas nor for the intervening dead layer between the pressure vessel walls and the sensitive volume. This is compounded by the multiple scattering within the pressure vessel which reduces otherwise energetic photons (which would ordinarily escape detection) to soft x-rays which are readily absorbed in the sensitive region. This trend is identical to that reported[8] earlier for background simulations of another detector.

4.2. Particle Background

Particles entering the active volume can also produce background events. However, energetic charged particles should be readily identified by the extended ionization tracks they produce in the sensitive volume using the imaging capabilities of the GSPC, by the long signal risetimes of such events, and by the large amount of total charge deposited. Long track and long signal risetime events are rejected in ground processing while large energy depositions will trigger on-board termination of event processing with no information entered into the telemetry stream. Low energy charged particles, those with paths traversing only a small section of the active volume, and neutral particles cannot be so easily identified. If numerous events of this nature occur and are not rejected on-board, they may potentially saturate telemetry.

Figure 9 shows the spectrum of charged particles incident upon the active region. The spectra are qualitatively similar to those displayed in figure 4 for transmittance through a typical Stainless Steel layer though the electron flux has increased by an order of magnitude at low energies. These are mainly recoil electrons from Compton scattering in the materials outside the active volume (further evidence for downscattering of energetic photons). Electrons enter

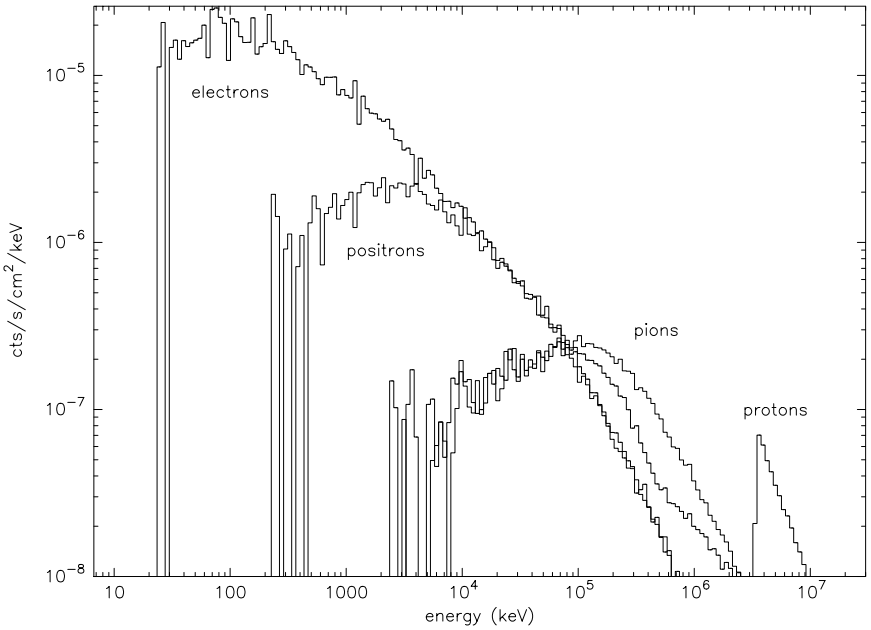

Figure 9. Particle background spectra in GSPC sensitive volume. Most energetic charged particles will deposit sufficient energy to trigger on-board rejection. Most neutrons will pass through the Xe fill gas undetected.

the active volume at a rate of 20 cts-s^{-1} though only 0.015 cts-s^{-1} have energies below 75 keV. Similarly, energetic $\pi^{\pm}$ and p^{+} enter at rates of 30 cts-s^{-1} and nearly all should be rejected on-board by exceeding the energy threshold.

Cosmic ray protons and atmospheric neutrons enter the active volume at rates similar to their respective external source rates. In addition, protons generate cosmic-ray showers of particles of various species; accounting for most of the flux shown in figure 9. The majority of these showers originate in the electronics housing and in the thick bottom flange of the pressure vessel. The remaining showers occur in the top and sides of the pressure vessel and in the ceramic fixtures.

Neutrons rarely interact. Most neutron interactions are capture reactions producing energetic (E ~1 MeV) de-excitation radiations which escape undetected. Neutron elastic scattering and delayed β-decays, known to be important background sources in solid state detectors,[4] were found to be unimportant in the Xe gas detector.

5. DISCUSSION

Numerical simulations reported here show that the dominant source of background in the as-built GSPC detector is leakage through the pressure vessel walls of diffuse cosmic gamma-ray and atmospheric background photons. According to one-dimensional slab simulations, the addition of 0.3 cm Pb passive shielding should reduce the shield leakage flux by an order of magnitude in the 40-200 keV energy range. Simulations of the entire detector, however, predict a much more modest reduction of ~27% to a level of ~0.0043 cts-s^{-1}-cm^{-2}-keV^{-1} in the 15-50 keV sensitive range. This is reconciled by the fact that hard x-rays penetrating the (shielded or unshielded) detector are subsequently downscattered to detectable energies by Compton scattering within the pressure vessel. The amount of shielding needed to prevent hard x-ray penetration, besides greatly exceeding payload weight limitations, would instead become sources of photon production through hadronic interactions in the high-Z shielding mass as confirmed by the slab simulations. Because of the discrepancies between the slab model predictions and the full model results, however, the precise thickness at which photon production begins to dominate cannot be quantified without full model simulations with thicker shielding layers which have yet to be performed. The instruments will be flown with 0.3 cm Pb shielding.

The addition of a 15 cm collimating tube can reduce the aperture flux component of the GSPC background by 90% to ~5×10^{-3} cts-s^{-1}-cm^{-2}-keV^{-1}. As bright galactic sources are typically 0.1 cts-s^{-1} or less at a focussed spot of half-power diameter ~0.05 cm, the expected signal-to-noise ratio is on the order of 5 or better.

Particle background is expected to be 20 cts-s^{-1} in electrons and higher in pions and protons but the vast majority of these should be rejected on-board by exceeding the upper energy threshold. Many of the remaining particle events should be rejected in post-flight processing though this simulation has not been undertaken. According to simulations reported here, the GSPC is not sensitive to the neutron flux as are solid state detectors in which elastic scattering and β-emission are important contributors to background noise.

Considerable effort has been made to realistically model the detector and external sources though no nearby payload masses were included in the simulations with the exception of the attached electronics housing. Operating at a float altitude corresponding to $\sim$3 g-cm^{-2} in directions towards the zenith, nearby structures could represent a substantial external source of photons and neutrons.[7] The largest of these is the accompanying EXITE experiment[12] which subtends approximately 0.4 str at $\sim$60 g-cm^{-2}. The spectral signature of photons produced in these nearby payload structures should be similar to the production spectra computed here for the pressure vessel (see, for example, figure 3) and should be treated as an additional component of the external radiation source described in § 2.2. This new component is flatter than the adopted $E^{-1.78}$ power law, extends to lower energies, and has a steep cut-off above a few to 10 MeV (depending on composition of the production materials). The photon intensity is, of course, unknown without quantitative modeling. Based upon earlier simulations[7] of induced background in a different detector flown under similar circumstances, nearby payload masses can be expected to increase the detected background but the shape of the detected background spectrum should remain similar to that computed here. Thus, the primary conclusions of this investigation; namely, the shape of the detected background spectrum, the dominance of shield leakage through the detector over photon production in the detector, and the relative differences among the three full-detector models considered here; should remain unchanged. These predictions will be tested in the future by comparing the results of these numerical simulations to flight data from the (shielded and collimated) GSPCs.

REFERENCES

1. R. A. Austin, B. D. Ramsey, C. L. Tse, and C. G. Zirnstein, "A high-pressure gas-scintillation-proportional counter for the focus of a hard x-ray telescope," in *EUV, X-Ray, and Gamma-Ray Instrumentation for Astronomy X*, O. H. Siegmund and K. A. Flanagan, eds., *Proc. SPIE* **3765**, pp. 714–720, 1999.
2. B. D. Ramsey, D. E. Engelhaupt, C. O. Speegle, S. L. O'Dell, R. A. Austin, J. J. Kolodziejczak, and M. C. Weisskopf, "HERO: High Energy Replicated Optics for a hard-x-ray balloon payload," in *EUV, X-Ray, and Gamma-Ray Instrumentation for Astronomy X*, O. H. Siegmund and K. A. Flanagan, eds., *Proc. SPIE* **3765**, pp. 816–821, 1999.
3. B. D. Ramsey, J. A. Apple, R. A. Austin, R. F. Elsner, D. E. Engelhaupt, J. J. Kolodziejczak, S. L. O'Dell, C. O. Speegle, D. A. Swartz, M. C. Weisskopf, and C. G. Zirnstein, "HERO: High Energy Replicated Optics for a hard-x-ray balloon payload," *X-Ray Optics, Instruments, and Missions IV*, R. B. Hoover and A. B. C. Walker II, eds., *Proc. SPIE* **4138**, 2000.
4. N. Gehrels, "Instrumental background in balloon-borne gamma-ray spectrometers and techniques for its reduction," *NIMS* A239, 324-349, 1985.
5. T. W. Armstrong, K. C. Chandler, and J. Barish, *J. Geophys. Res.* 78, 2715, 1973.
6. A. M. Prezler, S. Moon, and R. S. White, *J. Geophys. Res.* 81, 4715, 1976.
7. T. W. Armstrong, and B. L. Colborn, *Science Applications Report* SAIC-TN-96070, 1996.
8. B. D. Ramsey, C. R. Bower, K. L. Dietz, and M. C. Weisskopf, "The background in a balloon-borne fluorescence-gated proportional counter," *EUV, X-Ray, and Gamma-Ray Instrumentation for Astronomy*, *Proc. SPIE* **1344**, pp. 82–90, 1990.
9. GEANT Detector Description and Simulation Tool, Applications Software Group, Computing and Networks Division, CERN Program Library W5013, 1993.
10. J. O. Johnson, and T. A. Gabriel, *A User's Guide to MICAP: A Monte Carlo Ionization Chamber Analysis Package*, ORNL Technical Report TM-10340, 1988.
11. P. A. Aarnio, *Fluka user's guide*, CERN Technical Report TIS-RP-190, 1990.
12. R. P. Manandhar, K. S. Lum, S. S. Eikenberry, M. Krockenberger, and J. E. Grindlay, "Development of EXITE2: a large-area imaging phoswich detector/telescope for hard x-ray astronomy," *EUV, X-Ray, and Gamma-Ray Instrumentation for Astronomy IV*, *Proc. SPIE* **2006**, pp. 200–210, 1993.